



OPEN

Explainable artificial intelligence with UNet based segmentation and Bayesian machine learning for classification of brain tumors using MRI images

K. Lakshmi¹, Sibi Amaran², G. Subbulakshmi³, S. Padmini⁴, Gyanenedra Prasad Joshi^{5✉} & Woong Cho⁶

Detecting brain tumours (BT) early improves treatment possibilities and increases patient survival rates. Magnetic resonance imaging (MRI) scanning offers more comprehensive information, such as better contrast and clarity, than any alternative scanning process. Manually separating BTs from several MRI images gathered in medical practice for cancer analysis is challenging and time-consuming. Tumours and MRI scans of the brain are exposed utilizing methods and machine learning technologies, simplifying the process for doctors. MRI images can sometimes appear normal even when a patient has a tumour or malignancy. Deep learning approaches have recently depended on deep convolutional neural networks to analyze medical images with promising outcomes. It supports saving lives faster and rectifying some medical errors. With this motivation, this article presents a new explainable artificial intelligence with semantic segmentation and Bayesian machine learning for brain tumors (XAISS-BMLBT) technique. The presented XAISS-BMLBT technique mainly concentrates on the semantic segmentation and classification of BT in MRI images. The presented XAISS-BMLBT approach initially involves bilateral filtering-based image pre-processing to eliminate the noise. Next, the XAISS-BMLBT technique performs the MEDU-Net+ segmentation process to define the impacted brain regions. For the feature extraction process, the ResNet50 model is utilized. Furthermore, the Bayesian regularized artificial neural network (BRANN) model is used to identify the presence of BTs. Finally, an improved radial movement optimization model is employed for the hyperparameter tuning of the BRANN technique. To highlight the improved performance of the XAISS-BMLBT technique, a series of simulations were accomplished by utilizing a benchmark database. The experimental validation of the XAISS-BMLBT technique portrayed a superior accuracy value of 97.75% over existing models.

Keywords Brain tumors, Hyperparameter tuning, Explainable artificial intelligence, Semantic segmentation, Bayesian machine learning

The improper and uncontrolled growth of brain cells could result in BT formation. BTs are the main reason for death from cancer in those below 19 of age, comprising 24% of most of the deaths generated by cancer¹. There are nearly 120 different types of BTs. As a primary consequence, diagnosing an efficient treatment for particular kinds of BTs becomes more complicated. BTs might be classified into two principal sub-types: malignant and benign². Benign BTs are less cancerous than their malignant colleagues. After discussing the several types of cancer, the term “benign” indicates a tumour that doesn't spread or metastasize to other body parts. Various

¹Department of Information Technology, Sri Manakula Vinayagar Engineering College, Madagadipet, Puducherry, India. ²Department of Computing Technologies, School of Computing, College of Engineering and Technology, Faculty of Engineering and Technology, SRM Institute of Science and Technology, SRM Nagar, Kattankulathur, Chennai 603203, India. ³Department of Artificial Intelligence and Data Science, St. Joseph's College of Engineering and Technology, Elupatti, Thanjavur, India. ⁴Department of Computing Technologies, SRM Institute of Science and Technology, Kattankulathur, Chennai 603203, India. ⁵Department of AI Software, Kangwon National University, Samcheok, Republic of Korea. ⁶Department of Electronics, Information and Communication Engineering, Kangwon National University, Samcheok, Republic of Korea. ✉email: joshi@kangwon.ac.kr; wcho@kangwon.ac.kr

imaging conditions include positron emission tomography (PET), computed tomography (CT), single-photon emission CT (SPECT), MRI, and X-ray³. A three-dimensional image of the human brain can be obtained from a fixed MRI scan. The main persistence of this association is to recognize, investigate, categorize, and diagnose various neurological disorders. Radiation therapy has been generally utilized in cancer treatment, and MRI segmentation can often be applied to direct radiation therapy⁴. Because of this, it is possible to control whether or not a fragment identified by an MRI as a tumour is present. This treatment doesn't include ionizing radiation application and is instead employed for identification, diagnosing disease phases, and following monitoring⁵.

The most standard background in which this treatment is applied is within hospitals. MRI is the most advantageous condition currently available and is utilized to diagnose more innovative BT stages⁶. The growth of artificial intelligence (AI) and novel DL-based techniques have a significant influence on medical imaging, especially in diagnosing disease. The CNN method is the most widely applied DL technique in neural networks⁷. Features extraction and segmentation are the two characteristics of a conventional CNN model. The CNN architecture has five layers: a folding layer, an input layer, a pooling layer, a classification layer, and a fully connected (FC) layer⁸. KNN, ANN, and SVM are the most typically used and exact techniques. Simultaneously, increasing BT classification would require developing the obtainable data within the area and emerging a novel artificial neural network (ANN)-based DL technology⁹. The most prominent difference between these three tumours is that meningioma is naturally benign, while gliomas are usually malignant. CNNs are a neural network that aids you in visualizing, interpreting, and exploring vast data sizes in diagnostic imaging¹⁰. The recommended independent computer diagnostic algorithmic performance has been calculated using parameter precision.

This article presents a new explainable artificial intelligence with semantic segmentation and Bayesian machine learning for brain tumors (XAISS-BMLBT) technique. The presented XAISS-BMLBT technique mainly concentrates on the semantic segmentation and classification of BT in MRI images. The presented XAISS-BMLBT approach initially involves bilateral filtering (BF)-based image pre-processing to eliminate the noise. Next, the XAISS-BMLBT technique performs the MEDU-Net+ segmentation process to define the impacted brain regions. For the feature extraction process, the ResNet50 model is utilized. Furthermore, the Bayesian regularized ANN (BRANN) model is used to identify the presence of BTs. Finally, an improved radial movement optimization (IRMO) model is employed for the hyperparameter tuning of the BRANN technique. To highlight the improved performance of the XAISS-BMLBT technique, a series of simulations were accomplished by utilizing a benchmark database.

Review of literature

Cekic et al.¹¹ presented the Mask R-CNN structure, optimizing its advanced features to analyze and process the data from the preoperative microscope and surgical MRI videos. Resnet50 and Resnet101 support systems have been utilized in the method of Mask R-CNN, and experimenting outcomes have been provided. DL methods are trained from MRI and preoperative microscope images, and the classification outcome attained for every patient has been integrated by the average weight. Haq et al.¹² propose two proficient and fast BT classification methods based on deep CNNs by utilizing MRI data to detect and classify various kinds of BT. The author utilizes two freely accessible datasets from BraTS and Figshare 2018, employs restricted arbitrary regions to reduce forged outputs, and examines spatial data on well-segmentation tasks. Based on the Figshare dataset, the presented structure identifies BT as pituitary tumoursliomas or meningiomas. The following structure is separated among the grades of lower and higher gliomas (LGG and HGG, respectively). Rajendran et al.¹³ presented a technique that utilizes a gray level co-occurrence matrix features extraction method to remove redundant particulars from the images. In contrast with the present advanced technique, the precision of BT segmentation has been substantially enhanced by utilizing CNN, which is commonly used in segmenting biomedical images. By integrating the outcomes of 2 distinct segmentation systems, the presented technique determines a main but modest combinatorial tactic which, as a straight significance, produces more complete and precise evaluations. Jyothi and Singh¹⁴ aim to deliver a complete analysis of current mechanisms advanced in the segmentation of BT. In this study, an organized article analysis is proposed to the readers to recognize 3 strategies, specifically the conventional system, ML tactic, and DL method intended for the segmentation of BT. The main objective is to comprise conventional systems such as statistical-based methods and atlas-based strategies to segment tumours from brain MRI. Akter et al.¹⁵ presented a deep CNN-based structure for automated brain image identification into four modules and a U-Net-based segmentation method. Utilizing six benchmark datasets, the author tested the classifier and trained the segmentation method, allowing lateral comparison of the segmentation effect on tumour identification in brain MRI images. The advanced new DL-based method for BT segmentation and classification overtakes present pre-trained methods throughout six datasets.

Anantharajan et al.¹⁶ propose a new hybrid technique incorporating personalized features with CNNs to improve the performance of BT segmentation. In this research, personalized features are extracted from MRI scans, which include texture-based, shape-based, and intensity-based features. Simultaneously, a single CNN structure has been trained and developed to identify the features from the data spontaneously. The presented hybrid technique has been integrated with personalized features and features recognized by CNN in various ways for a novel CNN. Mohanty et al.¹⁷ propose a unique DL method, which restrains the strength of a soft attention mechanism, and accurately intended CNN has been employed. It contains four convolution layers. Most of the crucial inventions in the method represent the technique of extracting features. Rather than feature extraction uniquely from the concluding layer, as is usual in various methods, the technique combines and aggregates features from every layer. This assures that the crucial features inherent to every layer are not misplaced but combined into a comprehensive and robust feature vector. Mehnatkesh et al.¹⁸ present an optimizer-based deep convolutional ResNet method integrated with a new evolutional method to enhance the hyperparameters and structure of the deep ResNet method spontaneously without the necessity of human professionals. Also, the

physical structure design made identifying various kinds of BT difficult. In addition, according to the theories of difference development tactics and multiple-population operators, an enhanced version of IACO has been proposed. Amiya et al.¹⁹ develop a hybrid methodology that integrates GLCM for feature extraction and AlexNet for classifying low bone mass variations in DEXA images, assisting in the segmentation and diagnosis of osteoporosis, osteopenia, and normal bone health. Subramanian and Govindaraj²⁰ present an interactive toy using DL (HARNet) and IoT to teach yoga to autistic children, helping them improve social interaction. The toy responds to touch sensors and recognizes yoga postures to guide the child. Amiya et al.²¹ enhanced a texture feature extraction system that integrates local binary patterns (LBP) and normalized grey-level co-occurrence matrix-based (nGLCM) for volumetric images, with modified U-Net (ModU-Net) used for segmenting low bone mass in osteoporosis X-ray images. Shi et al.²² propose an SGS method by integrating SqueezeNet with a Gaussian kernel SVM for non-linear classification, attaining high accuracy and sensitivity in diagnosing COVID-19 from CT images.

Bouguerra et al.²³ propose a two-stage approach for BT classification, improving MRI images and combining model predictions utilizing ensemble learning for improved accuracy. Wang et al.²⁴ present RanMerFormer, a novel CAD method for BT classification by employing a pre-trained vision transformer. It integrates a tokenmerging mechanism for enhanced efficiency and a randomized vector functional link for fast training. Saeed et al.²⁵ introduce a three-phase method using DeeplabV3+ for segmentation, feature extraction with Darknet53 and MobileNetV2 for SVM, and XAI for analyzing features, with uncertainty quantified by confusion entropy. Alagarsamy et al.²⁶ developed an automated methodology for accurate BT prediction by incorporating the Firefly algorithm and interval type-II fuzzy logic system for improved tumour delineation in complex brain tissue. Nisha et al.²⁷ present an automated Alzheimer's disease detection system using MRI data, with pre-processing, brain tissue segmentation, and multiclass classification by utilizing hybrid dense optimal capsule network (Hybrid D-OCapNet), optimized by modified bald eagle search (M-BES) model. Rahman et al.²⁸ present Glioma-CNN, a lightweight model that integrates with gradient boosting. Interpretability is ensured through SHapley Additive exPlanations (SHAP) and Gradient-weighted Class Activation Mapping (Grad-CAM++). Alagarsamy et al.²⁹ develop an approach by integrating the artificial bee colony (ABC) and Interval Type-II fuzzy logic system (IT2FLS) to delineate tumour regions, assisting oncologists in decision-making accurately. Charaabi et al.³⁰ present an XAI-enhanced framework for improving the interpretability of Deep Transfer Learning (DTL) models in BT classification using MRI, leveraging pre-trained models like Xception, ResNet50-V2, DenseNet121, and EfficientNetB0-V2. Rajeev et al.³¹ develop a DL-based classification model comprising skull-stripping, tumour segmentation, feature extraction using improved Gabor wavelet transform (IGWT), feature selection with black widow adaptive red deer optimization (BWARD), and classification through a hybrid Elman BiLSTM network. Hosny et al.³² propose an ensemble approach using TL with DenseNet121 and InceptionV3, incorporating modified classifiers and Grad-CAM. Mallampati et al.³³ present an ML-based approach for BT detection using MRI features. It integrates 3D-UNet and 2D-UNet segmentation with KNN and gradient-boosting classifiers in a hybrid model using soft voting to enhance performance.

Khosravi et al.³⁴ aim to explore the integration of AI in anomaly detection for MRI, focusing on advanced ML and DL techniques to enhance diagnostic accuracy. Hossain et al.³⁵ aim to develop a TL-based multiclass classification model, IVX16, for faster and more reliable BT detection using MRI images, focusing on several DL architectures to improve tumour-type classification. Nag et al.³⁶ incorporate ResNet50 for feature extraction and Generative Adversarial Networks (GANs) for data augmentation. Halder et al.³⁷ aim to enhance automated BT diagnosis using DL and TL, integrating image denoising, tumour detection, and classification to improve accuracy and assist in early abnormality detection. Lamba and Rani³⁸ propose a novel brain-computer interface framework by integrating Xception architecture with TL for feature extraction and linear SVM for classification, enhanced by Gradient-Weighted CAM (Grad-CAM)-based Explainable AI for transparent brain-related diagnostics in smart healthcare. Roy et al.³⁹ review the role of explainable deep learning (XDL) and XAI in enhancing transparency and decision-making in medical imaging, aiming to bridge the gap in understanding DL models for healthcare applications. Chauhan et al.⁴⁰ compare DL models, including U-Net, PSPNet, DeepLabV3+, and ResNet50, for BT segmentation. Bidkar et al.⁴¹ propose a novel BT segmentation and classification techniques utilizing AdamSTBO+UNet++ for segmentation and Adam Salp Water Wave Optimisation with the Deep CNN (AdamSWO-DCNN) for classification, incorporating Adam optimizer with Sewing Training Based Optimization (STBO) and SWO. Shafiq and Butt⁴² focus on the utilization of U-Net for brain MRI segmentation, highlighting its efficiency in detecting key brain regions and exploring recent advancements in DL for medical image segmentation. Nirmalapriya et al.⁴³ introduce an optimization-driven model for BT classification, integrating U-Net and CFPNet-M for segmentation, trained by utilizing an aquila spider monkey optimization (ASMO) model and classifying tumours with a SqueezeNet model optimized by fractional ASMO (FASMO). Mithun and Jawhar⁴⁴ propose a YOLO NAS-based model, which utilizes hybrid anisotropic diffusion filtering for noise removal, encoder-decoder network (En-DeNet) for segmentation, and DL techniques for classification. Cao et al.⁴⁵ propose MBANet, a 3D CNN with multi-branch attention, utilizing an optimized shuffle unit and 3D Shuffle Attention modules for improved feature extraction and resolution recovery in BT detection.

Many studies on BT detection need to be revised, as well as computational complexity and dataset reliance limitations. Techniques like Mask R-CNN and GLCM for feature extraction may need help with high-complexity images or limited datasets, affecting accuracy and scalability. DL methods, namely CNNs and U-Net, are prone to overfitting on small datasets and need substantial computational resources. Hybrid methods that integrate personalized features with CNNs can be challenging to integrate effectively, reducing interpretability. Attention mechanisms and optimization techniques may increase model complexity, making them less suitable for real-time applications. Additionally, methods focused on specific imaging modalities may need to be better generalized to diverse medical data. The research gap is in developing more generalized, efficient models for

BT detection that can handle varied and complex datasets without overfitting while reducing computational complexity. Additionally, there is a requirement for methods that can seamlessly integrate multiple feature types and imaging modalities to enhance accuracy and real-world applicability.

Material and methods

This article presents a novel XAISS-BMLBT technique. The technique mainly concentrates on semantic segmentation and classification of BT in MRI images. It encompasses distinct pre-processing, segmentation, feature extractor, classification, and parameter tuning processes. Figure 1 illustrates the workflow of the XAISS-BMLBT technique.

Pre-processing: BF model

Initially, the presented XAISS-BMLBT approach involves BF-based image pre-processing to eliminate the noise present within it⁴⁶. This model is chosen for pre-processing because it can efficiently reduce noise while conserving edges in an image. Unlike conventional linear filters, which blur edges along with noise, BF utilizes diverse weights for neighbouring pixels based on their spatial distance and intensity difference. This confirms that only pixels with similar intensity values are averaged, preserving crucial details such as boundaries and textures. Furthermore, BF is computationally effectual and can be easily adjusted via its spatial and range parameters to suit diverse types of noise and image characteristics. This makes it versatile for image pre-processing tasks like segmentation, where edge preservation is critical. Figure 2 specifies the working flow of the BF technique.

It combines the image of input through weights calculated based on either intensity or geometric distances among the pixels of a neighbour. After a numerical viewpoint, BF functions as described in Eq. (1). $O(x, y)$, and $I(x, y)$ are the output and input pixels for the (x, y) coordinate; correspondingly, Ω represents $k \times k$ filtering window placed in $I(x, y)$; $Wr(i, j)$ and $Ws(i, j)$, are specified in Eq. (2), which means the range and spatial coefficients at the common location (i, j) in Ω .

$$O(x, y) = \frac{\sum I(i, j) \times Ws(i, j) \times Wr(i, j)}{\sum Ws(i, j) \times Wr(i, j)} \quad (1)$$

$$Ws(i, j) = e^{-\frac{(x-i)^2 + (y-j)^2}{2 \times \sigma_s^2}} \quad (2)$$

$$Wr(i, j) = e^{-\frac{|I(x, y) - I(i, j)|^2}{2 \times \sigma_r^2}} \quad (3)$$

It should be stated that the weight computation, which depends upon the Gaussian distribution, contains standard deviation parameters σ_r and σ_s that have been utilized as fine-tuning parameters to modify the filtering level. Mainly, σ_s represents a set based upon the size of the filtering window, hence that $\sqrt{(x-i)^2 + (y-j)^2} \leq 3 \times \sigma_s$ equally, σ_r must be accurately selected based on the task to perform. For instance, regarding the denoising, its value is based upon the existing noisy standard deviation σ_n , and it is chosen subsequently $\sigma_r = 3 \times \sigma_n$.

For Eqs. (1)–(3), the BF difficulty is mainly owing to the significant number of multiplication and exponentiation processes required to calculate the filter's weight. If it is alone, the spatial coefficients can be regarded as constant once k represents a set; alternatively, the coefficients of the range need additional computing sources to execute exponential operations at the timeline for various pixel intensity variations and σ_r .

Segmentation: MEDU-Net+ technique

Next, the XAISS-BMLBT technique utilizes the MEDU-Net+ segmentation to define the impacted brain regions⁴⁷. The MEDU-Net+ technique is selected for segmentation because it can effectively capture fine and coarse features through a multi-scale architecture. This model builds on the popular U-Net framework, improving it with additional encoding-decoding layers and skip connections, which allow it to preserve spatial data while enhancing segmentation accuracy. MEDU-Net+ also incorporates multi-level attention mechanisms, enabling it to concentrate on relevant regions while suppressing irrelevant background noise. Compared to other models, it is highly effective in handling intrinsic structures and weakly-defined boundaries, making it appropriate for medical image segmentation tasks. Its flexibility, performance in diverse contexts, and robust generalization capabilities make it an ideal choice.

Recently, the U-Net-based medical image segmentation has attracted much attention, and various improved U-Net networks are presented gradually, like U-Net++, V-Net, Multi-ResU-Net, 3D U-Net, U2-Net, and CE-Net. Some better techniques mostly advance the basic convolution block during the encoding, add residual connections between convolution blocks, or widen and deepen the network. Nevertheless, this method often carries the parameters increase energetically.

It differed from the preceding improved U-Net networks, which only develop the encoder and the connection; the suggested MEDU-Net+ network incorporates the information between encoding and decoding and progresses the decoder, encoder, and skip connection to accomplish superior performance. The recommended MEDU-Net+ network even utilizes the U-shaped architecture. Compared with U-Net, the presented network performance is significantly improved, and the parameter counts have an assured rise. Then, the U-shaped framework has been filled with the deconvolution transmission term.

The suggested MEDU-Net+ comprises the multi-scale encoder joined with Google Net; the novel layer-wise skip connection, and the multiple-scale feature fusion of the decoder. The encoding block function removes image feature information over a sequence of operations like pooling and convolution. This block comprises four

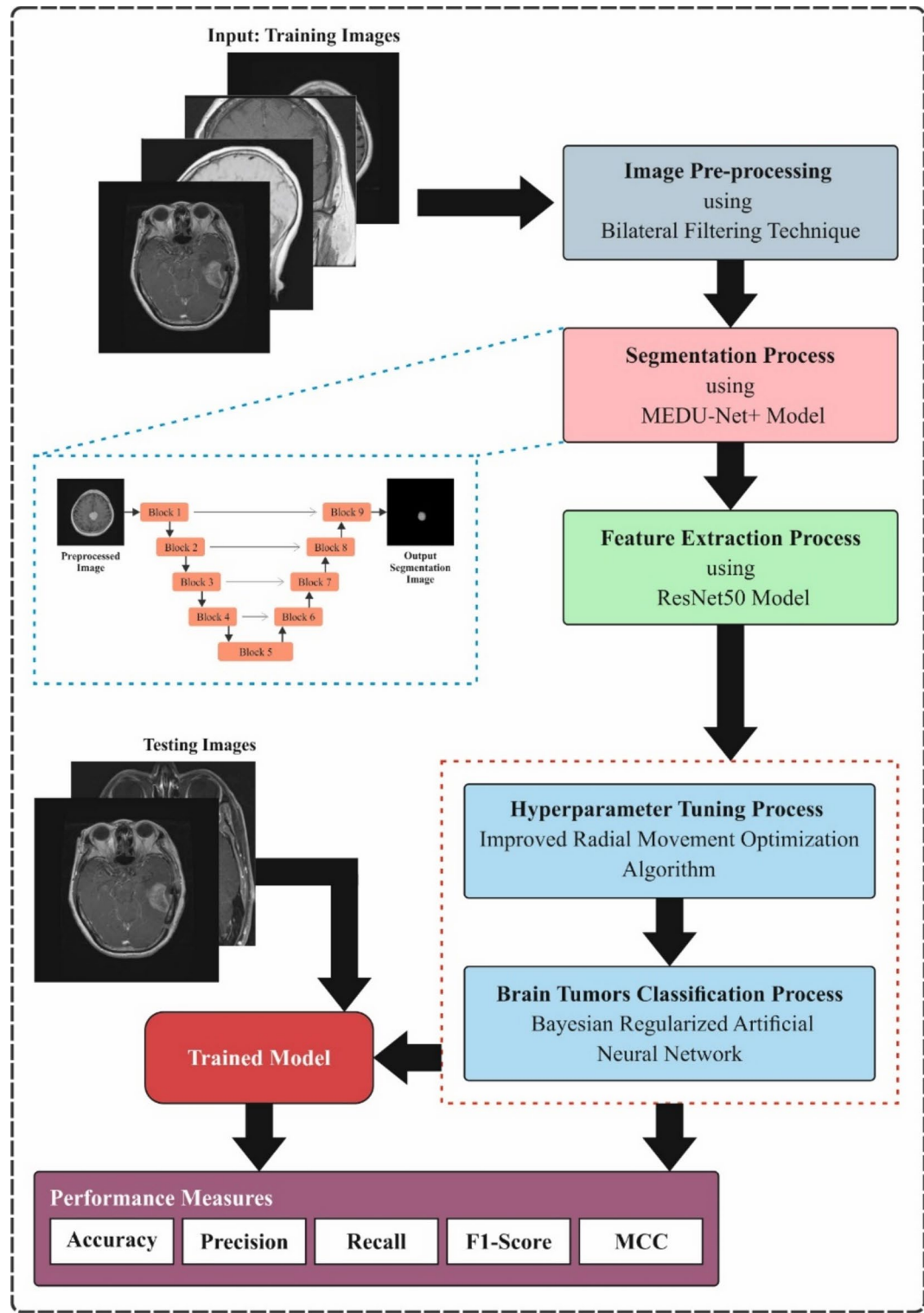


Fig. 1. Workflow of XAISS-BMLBT technique.

sub-modules, every submodule holding four branches: 1×1 convolution, the concatenation 1×1 convolution and 3×3 convolution, the concatenation 1×1 convolution and 5×5 convolution, and the concatenation 3×3 maximum pooling and 1×1 convolution. The output is the outcome of concatenating these four branches. After every sub-module, a down-sampling layer can be applied through the maximum pooling that successively gathers deeper semantic information. This connection block presents a novel layer-wise returned skip connection that creates a more proper route for transferring information between encoder and decoder through the essential stages of connection, convolution, and deconvolution. The layer-wise skip connection can be understood

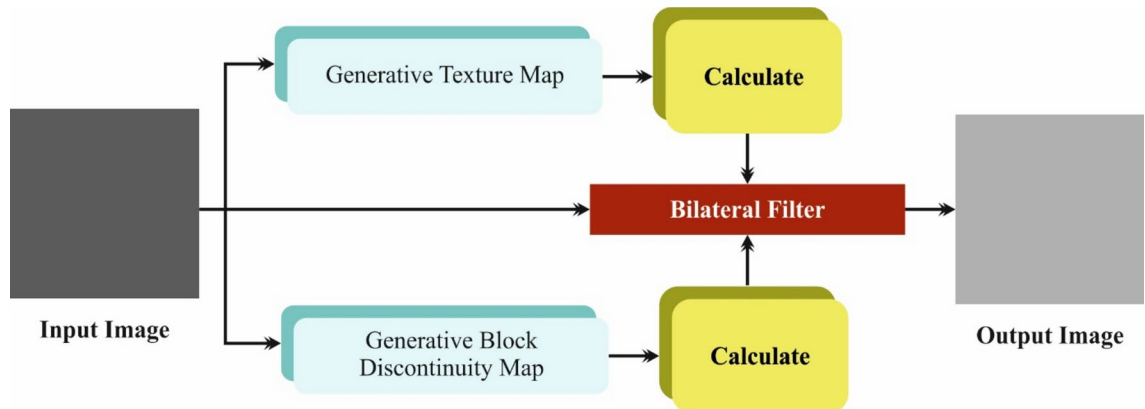


Fig. 2. Workflow of BF technique.

as a flow of many *U*-shaped networks, utilizing this transmission form to transmit and collect semantical information of each coding layer. The consistent decoder block contains four layers, each with a sub-module from deconvolution and up-sampling. Various scales of convolution of 1×1 , 3×3 , and 5×5 are selected to deconvolution the information. The outcomes of every branch further aggregate to gain the output of every deconvolution block by the decoder. Throughout decoding, the resolution can be stored by up-sampling till it is reliable with the resolution of the input image. The complete contributions of the presented MEDU-Net+ are assumed below:

1. The inception structure of the above-mentioned Google Net convolution block replaces the encoding convolution block of the MEDU-Net+. These inception frameworks contain four branches: the 1×1 convolution, the concatenated 1×1 and 3×3 convolutions, the concatenated 1×1 and 5×5 convolutions, and the concatenated 3×3 max pooling and 1×1 convolution. Then, the output of the encoder convolution block is the outcome of the concatenation of the four branches.
2. A novel skip connection in the suggested MEDU-Net+ network is presented. The layer-wise skip connection includes a transferring item depending on deconvolution and a drop of several *U*-shaped networks. Besides, these novel skip connection processes are connection, deconvolution, and convolution. Finally, all the gathered semantic information is aggregated.
3. Multiple scales feature fusion is presented to the decoder segment for receiving improved image segmentation performance. The receptive domains in the aggregation method are also significant, and the feature extraction is recovered more systematically by utilizing larger and different-scale receptive areas. Thus, they select convolution kernels of numerous sizes. The decoder part deconvolves the convolution kernel sizes of 1×1 , 1×1 and 3×3 and 5×5 , after that, combines the outcomes of every branch to attain the output of the basic block of deconvolution. Usually, the presented network has a unique key structure without a redundant branch structure. This new network architecture has significant flexibility and is suitable for adding modules to develop the performance further.

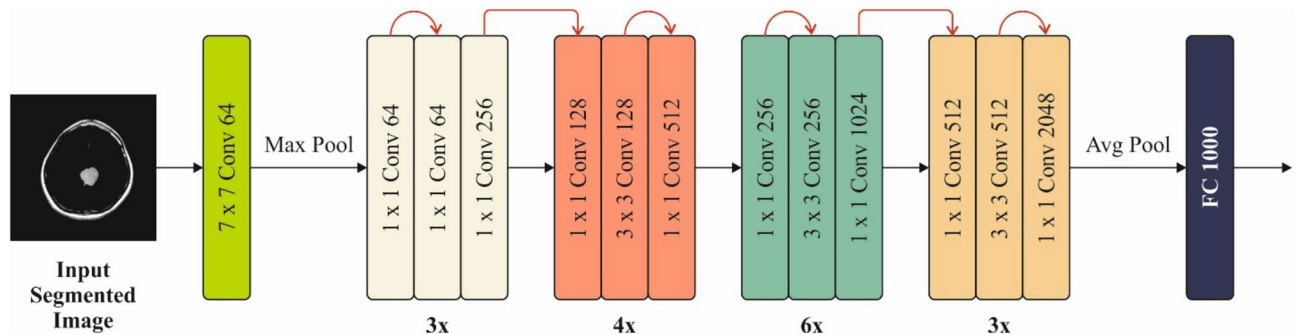
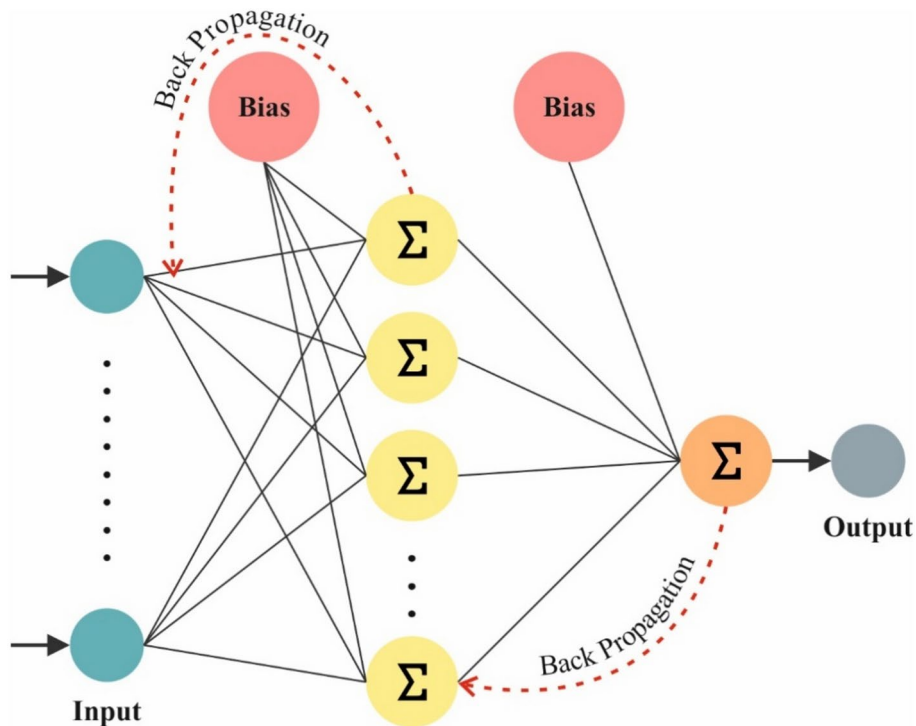
Feature extractor: ResNet50 model

For the feature extraction process, the ResNet50 model is employed⁴⁸. This model is chosen due to its deep residual learning architecture, which effectually reduces the vanishing gradient problem and enables the training of intense networks. The 50-layer depth allows it to capture complex hierarchical features in images, making it specifically appropriate for complex tasks such as medical image analysis. Its residual blocks facilitate the learning of more robust representations without suffering from degradation in performance as the network deepens. Additionally, ResNet50 has been widely validated in various image classification and feature extraction tasks, showing robust generalization capability and high accuracy. Compared to shallower models, ResNet50 presents superior performance in extracting meaningful features from high-dimensional data. Its pre-trained versions also provide a crucial advantage in transfer learning (TL) scenarios, reducing the requirement for large training data. Figure 3 defines the framework of the ResNet50 model.

ResNet50's main feature is the use of remaining connections to struggle with the problem of vanishing gradients in training complex networks. With 50 layers, ResNet50 integrates batch normalization (BN), max-pooling, convolutional layers, and FC layers in a hierarchical structure. Its remaining blocks discriminate ResNet50, which represents the theory of residual learning. Every block covers dual 3×3 convolutional layers with BN, *ReLU*, and a shortcut link to acquire across a layer. This design permits a smoother data flow within the network, making it simpler to train much deeper structures. Furthermore, ResNet50 utilizes bottleneck blocks in its deeper layer to enhance model performance and computational efficacy. The design comprises a global average pooling layer to collect spatial data from the feature map and an FC layer for classification.

Classification process: BRANN model

Furthermore, the BRANN model is utilized to detect the presence of BTs⁴⁹. This model is chosen due to its capacity to incorporate the power of neural networks with Bayesian regularization, which enhances generalization and

**Fig. 3.** Framework of ResNet50 model.**Fig. 4.** BRANN architecture.

mitigates overfitting. By integrating a probabilistic framework, BRANN optimizes the network's weights through a penalty on large weights, resulting in a more robust and stable model. This regularization assists in cases where limited data is available or the dataset is noisy, which is common in real-world applications. Compared to conventional neural networks, BRANN presents a more reliable performance by balancing model complexity and accuracy. Also, the Bayesian approach provides a natural way to quantify uncertainty, making it ideal for applications needing confidence in predictions, such as medical diagnostics. Its flexibility and efficiency in handling non-linear relationships and intrinsic patterns make it a robust choice over conventional classification methods. Figure 4 demonstrates the structure of the BRANN model.

Unlike conventional ANN, BRANN integrates the Bayesian inference standards through ANN. It proposes a Bayesian regularization in the training process by increasing loss function by a further term. This additional term sentences the enormous weight that can be presented for providing a smooth network response. The function of loss can be presented in BRANN, which can be represented below:

$$L = \beta \frac{1}{N} \sum_i^N (Y_i^T - Y_i^P)^2 + \alpha \frac{1}{N} \sum_i^N w_i^2 \quad (4)$$

whereas w_i represents the weight of the network; β and α are loss function hyperparameters. When $\alpha > \beta$, the training method will focus on decreasing errors, resulting in small values of error. In contrast, if $\alpha < \beta$, training will give priority to decreasing the weight size, as it arises by the higher network error cost.

In BRANN, random variables rather than fixed values weigh the neural network weights. When the data is recovered, the function of density for the weight of ANN is upgraded based on the Bayes' rule is expressed below:

$$P(w|D, \alpha, \beta, M) = \frac{P(D|w, \beta, M) P(w|\alpha, M)}{P(D|\alpha, \beta, M)} \quad (5)$$

D represents the training data set, and M denotes a specific ANN method. $P(D|w, \beta, M)$ means the function of likelihood that computes the network weight probability. $P(w|\alpha, M)$ states the density of preceding that describes the data or principles regarding the weights before one data is gathered. $P(D|\alpha, \beta, M)$ are fed as normalizing factors to ensure that the overall probability adds up to 1.

With Bayesian inference, BRANN could evaluate the following distribution across the network parameters instead of detecting a single-point estimation. In the Bayesian structure, the optimum weights have been identified by increasing the posterior probability ($w|D, \alpha, \beta, M$). This maximizing method is equal to minimizing the regularized function of loss L .

Regularizing Bayesian in BRANN helps inhibit overfitting by striking a disadvantage on huge weights, promising a more generalized and robust method. In addition, the uncertainty estimations offered by BRANN are beneficial in decision-making, determining the uncertainty in predictions. BRANN has been used in different fields, including classification, regression, and reinforcement learning tasks.

Parameter tuning: IRMO model

Finally, an IRMO method is employed for the hyperparameter tuning of the BRANN model⁵⁰. This method is chosen due to its efficient search mechanism, which integrates the merits of radial-based movement with enhanced exploration and exploitation strategies. IRMO enhances conventional optimization algorithms by utilizing a radial movement approach that dynamically alters the search space, allowing it to escape local minima and converge to global optima more effectively. Compared to other optimization techniques, IRMO exhibits faster convergence rates and greater accuracy in finding optimal solutions for complex, non-linear problems. Its robustness in handling various parameter spaces, particularly in high-dimensional optimization tasks, makes it appropriate for fine-tuning ML models. Furthermore, IRMO's flexibility and adaptability across diverse domains, from neural networks to DL models, confirm its superior performance over conventional methods such as grid or random search. Figure 5 specifies the steps involved in the IRMO model.

The IRMO model is one global optimizer model employed to resolve the optimum values of a multidimensional objective function effectively. The data structure was enhanced and altered depending on the RMO method to



Fig. 5. Steps involved in the IRMO technique.

improve the self-feedback capability between particles. This certifies that the valued data of the particle swarm is repeatedly organic to discover the finest solution.

After describing the parameter variable and objective function, the algorithm of IRMO sets numerous particles at random. It then repeatedly hunts for the optimum solution by assessing the value and upgrading them depending on contrasts. The particle locations and the optimal solution aid as an initial centre location. In every subsequent group, new particles are generated near this vital fact. The function values are assessed and equated to the preceding group. This procedure includes repeatedly upgrading the optimum solution and vital location near the global optimal as the iteration grows. The global optimum solution has been signified by the value of the function, which matches the point where the space of the solution finally unites. The execution steps of the IRMO model are given below:

1. Create the initial population.
2. Initially, the lower limit $x_{\min,j}$ and upper limit $x_{\max,j}$ of every dimension variable are fixed by Eqs. (6) and (7), and N early position points X_i ($1 \leq i \leq N$) are produced at random as per Eq. (8). These early locations establish the early population X as definite in Eq. (9). In the calculation, M signifies the complete volume of variables. The global optimum position point $Gbestx^1$ has been computed for every position point X_i in the early population and selected as the early position centre $Centre^1$.

$$X_{\min} = [x_{\min,1} x_{\min,2} \dots x_{\min,M}] \quad (6)$$

$$X_{\max} = [x_{\max,1} x_{\max,2} \dots x_{\max,M}] \quad (7)$$

$$X_i = X_{\min} + rand(0, 1) \times (X_{\max} - X_{\min}) \quad (8)$$

$$X = \begin{bmatrix} x_{1,1} & x_{1,2} & \cdots & x_{1,M} \\ x_{2,1} & x_{2,2} & \cdots & x_{2,M} \\ \vdots & \vdots & \ddots & \vdots \\ x_{N,1} & x_{N,2} & \cdots & x_{N,M} \end{bmatrix} \quad (9)$$

3. Enhance the position information by refining the accuracy and details of the location data. The optimum position is where the objective function reaches its best value. It represents the most favourable solution within the solution space.
4. The pre-position Y_i^k is produced as per Eqs at the k th iteration. Equations (10) and (11), whereas β_1 and β_2 are randomly produced numbers from 0 to 1, and G refers to the highest iteration count. Once the pre-position Y_i^k is produced, the target function assesses its value, which is equated with the value of the objective function from the preceding group. Then, the location data equivalent to the optimum value is removed and chosen as the present optimum location, denoted as point $Rbest^k$. If the current location $Rbest^k$ demonstrates greater than the global optimum location $Gbest^{k-1}$, an upgrade is created to the global optimum location.

$$\text{if } \beta_1 < 0.1 \text{ or } \beta_2 < \beta, Y_i^k = Centre^{k-1} + rand(-0.5, 0.5) \times (X_{\max} - X_{\min}) w^k \quad (10)$$

$$\text{Otherwise, } Y_i^k = X_{i-1}^k \quad (11)$$

$$w^k = 1 - k/G \quad (12)$$

$$\beta = \frac{j}{M} \quad (13)$$

5. Change the location of the centre.
6. According to Eq. (14), the central location alters with the overall and global optimum locations. Once repeated to the latter group, the optimum location point $Centre^k$ is the last outcome. In the calculation, C_1 and C_2 denote the correlation coefficient that impacts the balance and the haste of convergence, where values typically range from 0.4 to 0.9. In this work, the values given to C_1 and C_2 are 0.4 and 0.5, correspondingly.

$$Centre^k = Centre^{k-1} + C_1 (Gbestx^k - Centre^{k-1}) + C_2 (Rbestx^k - Centre^{k-1}) \quad (14)$$

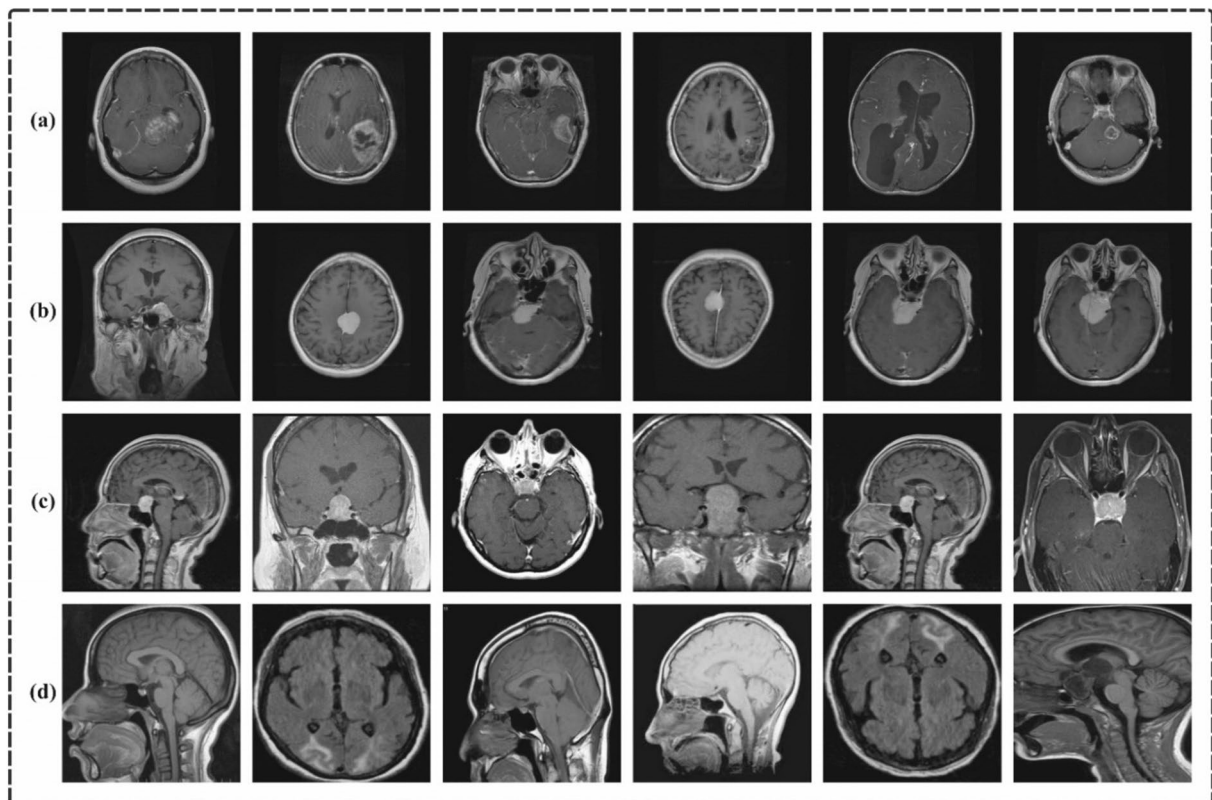
The IRMO model develops a fitness function (FF) to enhance classification performance. It explains a positive integer to describe the improved performance of the candidate solutions. In this work, the minimization of the classification rate of error can be determined as the FF, as presented in Eq. (15).

$$\begin{aligned} Fitness(x_i) &= ClassifierErrorRate(x_i) \\ &= \frac{\text{Number of misclassified samples}}{\text{Total number of samples}} \times 100 \end{aligned} \quad (15)$$

XAI: lime

LIME helps DL specialists describe some ML classifiers by highlighting the main input properties responsible for a prediction⁵¹. LIME interprets by approximating a black box method with an explainable technique. A

Classes	Image count
Glioma	1300
Meningioma	1300
No-tumor	1500
Pituitary	1400
Total count	5500

Table 1. Details of the dataset.**Fig. 6.** Sample images.

comprehensible depiction of images is a binary vector that signifies the absence or presence of a sequence of related connecting pixels (also termed superpixels). Equation (16) offers the description provided by LIME.

$$\xi(x) = \arg \min_{g \in G} \mathcal{L}(f, g, \pi_x) + \Omega(g), \quad (16)$$

An interpretation can be described as a method with various justification fidelity functions, families, and complex measures.

Experimental results and analysis

This article examines the stimulated validation analysis of the XAISS-BMLBT method by employing the BT-MRI dataset⁵², which contains 5500 samples with four classes in Table 1. Figure 6 defines the sample images. Figure 7 illustrates the original and segmented images. The suggested technique is simulated using the Python 3.6.5 tool on PC i5-8600k, 250 GB SSD, GeForce 1050Ti 4 GB, 16 GB RAM, and 1 TB HDD. The parameter settings are provided: learning rate: 0.01, activation: ReLU, epoch count: 50, dropout: 0.5, and batch size: 5.

Figure 8 reports a set of confusion matrices generated by the XAISS-BMLBT model on various epochs. On 500 epochs, the XAISS-BMLBT model has recognized 1217 samples into glioma, 1240 samples into meningioma, 1464 samples into no-tumor, and 1323 samples into pituitary. In addition, on 1000 epochs, the XAISS-BMLBT method has predicted 1224 samples into glioma, 1228 samples into meningioma, 1469 samples into no-tumor, and 1332 samples into pituitary. Meanwhile, on 2500 epoch counts, the XAISS-BMLBT techniques have identified 1199 samples into glioma, 1223 samples into meningioma, 1461 samples into no-tumor, and 1315

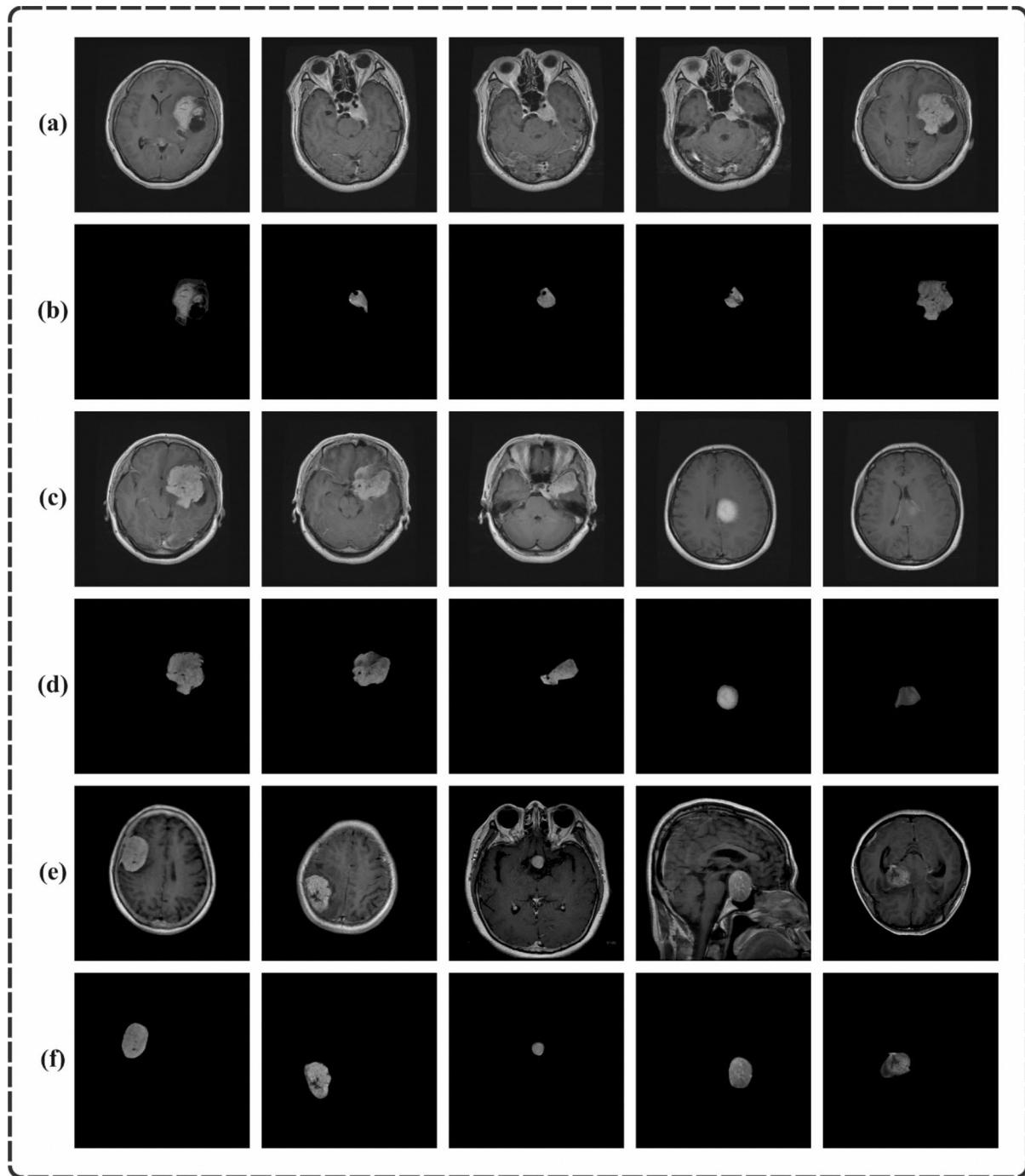


Fig. 7. (a,c,e) Original images and (b,d,f) Segmented images.

samples into pituitary. At last, on 3000 epoch counts, the XAISS-BMLBT approach has recognized 1186 samples into glioma, 1218 samples into meningioma, 1457 samples into no-tumor, and 1292 samples into pituitary.

Table 2 represents the overall BT detection results of the XAISS-BMLBT methodology with various epochs.

Figure 9 defines the classifier outcome of the XAISS-BMLBT approach under epochs 500–1500. The table values inferred that the XAISS-BMLBT approach has correctly identified four class labels. With 500 epochs, the XAISS-BMLBT model offers an average $accu_y$ of 97.67%, $prec_n$ of 95.36%, $reca_l$ of 95.27%, $F1_{score}$ of 95.31%, and MCC of 93.77%. Also, with 1000 epoch counts, the XAISS-BMLBT technique provides an average $accu_y$ of 97.75%, $prec_n$ of 95.56%, $reca_l$ of 95.42%, $F1_{score}$ of 95.48%, and MCC of 93.99%. Moreover, with 1500 epoch counts, the XAISS-BMLBT technique presents an average $accu_y$ of 97.48%, $prec_n$ of 95.02%, $reca_l$ of 94.87%, $F1_{score}$ of 94.93%, and MCC of 93.27%.

Figure 10 describes the classifier result of the XAISS-BMLBT technique under epoch counts 2000–3000. The table values gathered show that the XAISS-BMLBT technique correctly recognizes four classes. With 2000 epoch

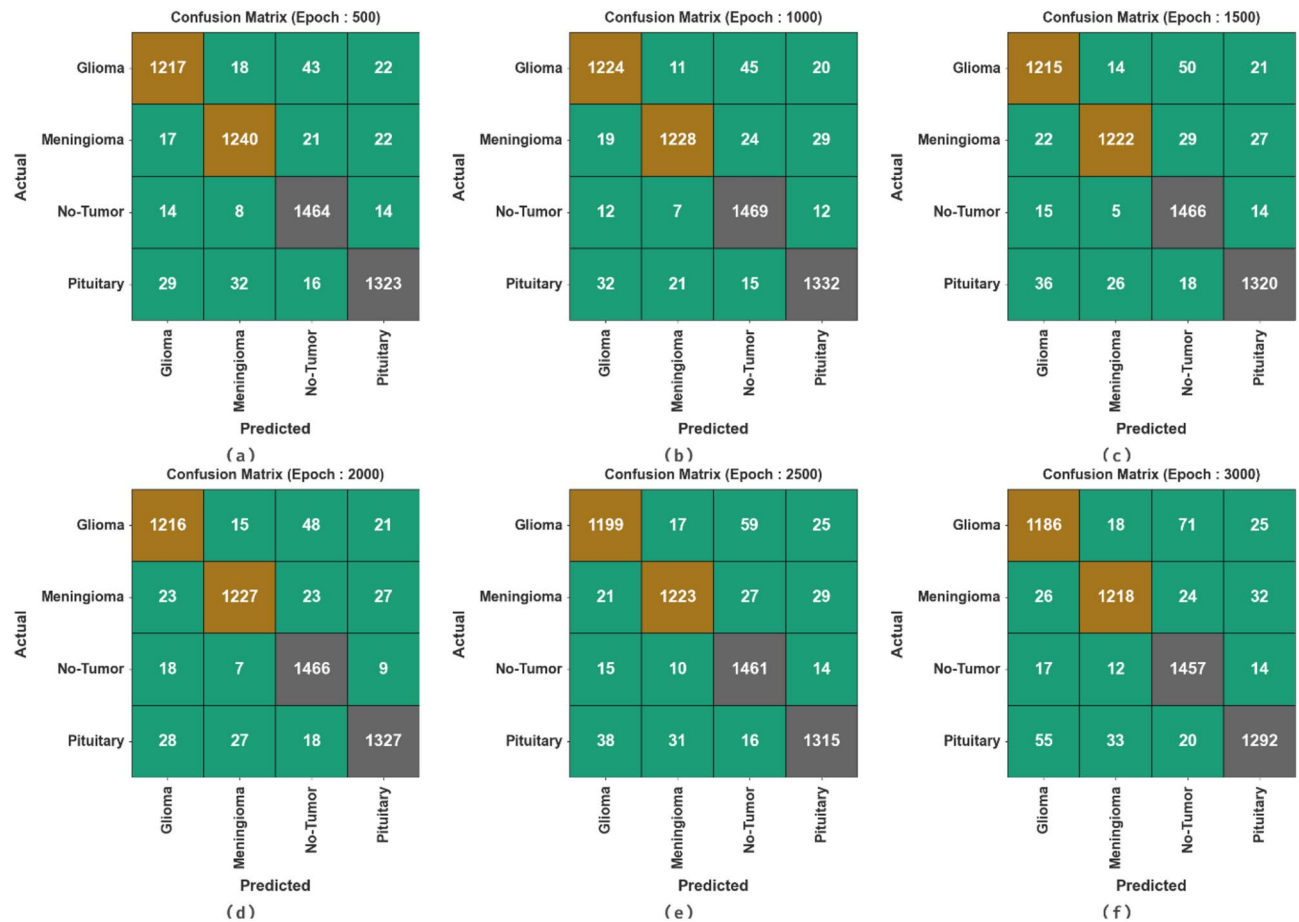


Fig. 8. Confusion matrices of XAISS-BMLBT technique (a-f) Epochs 500–3000.

counts, the XAISS-BMLBT approach provides an average acc_y of 97.60%, $prec_n$ of 95.24%, $reca_p$ of 95.11%, $F1_{score}$ of 95.16%, and MCC of 93.57%. Additionally, with 2500 epoch counts, the XAISS-BMLBT approach presents an average acc_y of 97.25%, $prec_n$ of 94.55%, $reca_p$ of 94.41%, $F1_{score}$ of 94.47%, and MCC of 92.65%. Finally, with 3000 epoch counts, the XAISS-BMLBT approach gives an average acc_y of 96.85%, $prec_n$ of 93.73%, $reca_p$ of 93.59%, $F1_{score}$ of 93.64%, and MCC of 91.56%.

Figure 11 states the training and validation accuracy results of the XAISS-BMLBT technique. The accurate outcomes are calculated for 0–3000 epochs. The figure underlines that the training and validation accuracy performance shows a reliable tendency that informed the proficiency of the XAISS-BMLBT methodology with greater values across various numbers of iterations. Additionally, the training and validation accuracy stayed nearer through the number of epochs that illustrate lower reduced overfitting and display better performance of the XAISS-BMLBT methodology, assuring steady prediction on unseen instances.

Figure 12 depicts the training loss and validation loss graph of the XAISS-BMLBT methodology. The loss outcomes are calculated over 0–3000 epochs. The training and validation accuracy performance has a reducing tendency, which reports the capacity of the XAISS-BMLBT approach to balancing a trade-off between data fitting and generalization. The consistent lessening in loss outcomes further ensures higher results for the XAISS-BMLBT approach and tuning the prediction results on time.

In Fig. 13, the precision-recall (PR) curve examination of the XAISS-BMLBT model explains its performance by plotting Precision against Recall for all the class labels. The figure expresses that the XAISS-BMLBT method constantly reaches superior PR values across various classes, representing its capability to preserve an essential proportion of true positive predictions between every positive prediction (precision) but additionally captures a greater portion of actual positives (recall). The gradual increase in PR results among all class labels indicates the efficiency of the XAISS-BMLBT method in the classification process.

Figure 14 shows the ROC curve of the XAISS-BMLBT method. The outcomes showed that the XAISS-BMLBT technique attains improved ROC results for all class labels, representing the critical ability to differentiate the class labels. These arising tendencies of enhanced ROC values over several class labels indicate the efficient performance of the XAISS-BMLBT approach in predicting class labels, emphasizing the robust nature of the classification process.

In Table 3 and Fig. 15, the stimulation values of the XAISS-BMLBT approach with existing methods are offered^{23,24,53–55}. The outcomes demonstrate that the novel 3D-CNN approach has presented poor performance with acc_y , $prec_n$, $reca_p$ and $F1_{score}$ of 89.50%, 92.02%, 90.40%, and 91.50%, correspondingly. Simultaneously,

Class	<i>Accu_y</i>	<i>Prec_n</i>	<i>Reca_p</i>	<i>F1_{Score}</i>	MCC
Epoch—500					
Glioma	97.40	95.30	93.62	94.45	92.76
Meningioma	97.85	95.53	95.38	95.46	94.05
No-tumor	97.89	94.82	97.60	96.19	94.75
Pituitary	97.55	95.80	94.50	95.15	93.51
Average	97.67	95.36	95.27	95.31	93.77
Epoch—1000					
Glioma	97.47	95.10	94.15	94.63	92.98
Meningioma	97.98	96.92	94.46	95.68	94.37
No-tumor	97.91	94.59	97.93	96.23	94.81
Pituitary	97.65	95.62	95.14	95.38	93.81
Average	97.75	95.56	95.42	95.48	93.99
Epoch—1500					
Glioma	97.13	94.33	93.46	93.89	92.02
Meningioma	97.76	96.45	94.00	95.21	93.76
No-tumor	97.62	93.79	97.73	95.72	94.11
Pituitary	97.42	95.51	94.29	94.90	93.17
Average	97.48	95.02	94.87	94.93	93.27
Epoch—2000					
Glioma	97.22	94.63	93.54	94.08	92.27
Meningioma	97.78	96.16	94.38	95.26	93.82
No-tumor	97.76	94.28	97.73	95.97	94.46
Pituitary	97.64	95.88	94.79	95.33	93.75
Average	97.60	95.24	95.11	95.16	93.57
Epoch—2500					
Glioma	96.82	94.19	92.23	93.20	91.13
Meningioma	97.55	95.47	94.08	94.77	93.17
No-tumor	97.44	93.47	97.40	95.40	93.66
Pituitary	97.22	95.08	93.93	94.50	92.64
Average	97.25	94.55	94.41	94.47	92.65
Epoch—3000					
Glioma	96.15	92.37	91.23	91.80	89.28
Meningioma	97.36	95.08	93.69	94.38	92.66
No-tumor	97.13	92.68	97.13	94.86	92.91
Pituitary	96.75	94.79	92.29	93.52	91.36
Average	96.85	93.73	93.59	93.64	91.56

Table 2. BT detection outcome of XAISS-BMLBT model under various epochs.

the Fine-tuned VGG19 method has gained marginally improved results with $accu_y$, $prec_n$, $reca_p$, and $F1_{score}$ of 94.00%, 93.03%, 91.71%, and 92.95%, individually. Also, the Inception-V3, Xception, Random Forest (RF), and ResNet50 techniques have obtained somewhat nearer performance. In the meantime, the graph CNN process has resulted in significant results with $accu_y$, $prec_n$, $reca_p$, and $F1_{score}$ of 96.65%, 93.30%, 91.78%, and 92.32%, appropriately. Furthermore, the EfficientNet-B5, DenseNet-169, RanMerFormer, and ResNet152V2 techniques attained slightly increased values. But the XAISS-BMLBT methodology outshines the other model with greater $accu_y$, $prec_n$, $reca_p$, and $F1_{score}$ of 97.75%, 95.56%, 95.42%, and 95.48%, correspondingly.

The execution timing (EXT) of the XAISS-BMLBT model is calculated using recent techniques in Table 4. The outcomes underscored that correspondingly, the novel 3D-CNN and Xception methods have gained low performance with improved EXT of 23.75 s and 22.14 s. As well as that, the Inception-V3, ResNet50, Fine-tuned VGG19, and Graph CNN methodology have stated adjacent EXT values of 19.08 s, 18.73 s, 16.92 s, and 12.43 s, respectively. In the meantime, the RF approach is accomplished to describe a significant EXT of 9.77 s. Moreover, the EfficientNet-B5, DenseNet-169, RanMerFormer, and ResNet152V2 approaches exhibited EXT values of 23.92 s, 25.58 s, 27.12 s, and 28.68 s. However, the XAISS-BMLBT methodology performed better with a minimum EXT of 4.60 s. Hence, the XAISS-BMLBT methodology is used to recognize BT automatically.

Conclusion

In this work, a new XAISS-BMLBT method is presented. The presented XAISS-BMLBT method mainly concentrates on the semantic segmentation and classification of BT in MRI images. It encompasses distinct pre-processing, segmentation, feature extractor, classification, and parameter tuning processes. The presented

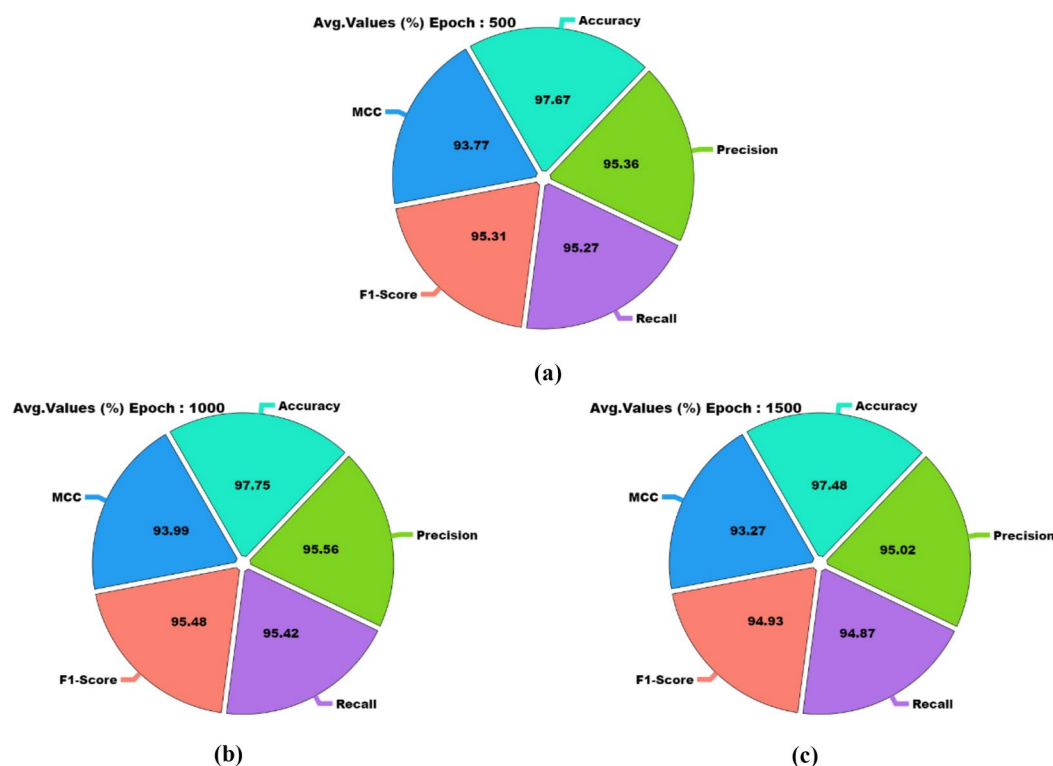


Fig. 9. Average outcome of XAISS-BMLBT approach (a–c) epochs 500–1500.

XAISS-BMLBT approach initially performed BF-based image pre-processing to eliminate the noise. Next, the XAISS-BMLBT approach utilized the MEDU-Net+ segmentation process to define the impacted brain regions. For the feature extraction process, the ResNet50 model is used. Furthermore, the BRANN model was employed to identify the presence of BTs. Finally, an IRMO technique was used for the hyperparameter tuning of the BRANN technique. To highlight the improved performance of the XAISS-BMLBT technique, a series of simulations were accomplished by utilizing a benchmark database. The experimental validation of the XAISS-BMLBT technique portrayed a superior accuracy value of 97.75% over existing models. The limitations of the XAISS-BMLBT technique comprise its reliance on a single dataset, which may limit the model's generalizability to diverse patient populations or imaging conditions. The study concentrates primarily on specific image processing techniques, which may not perform as well in extreme noise or artefacts. The computational complexity of the model also poses challenges for real-time applications, specifically in resource-constrained environments. Furthermore, while the proposed methodology shows promising results, it lacks a comprehensive evaluation across various clinical scenarios and external validation datasets. Future studies may explore incorporating multimodal data, such as patient demographics and clinical history, to enhance predictive performance. Moreover, further optimization of the model for faster processing and implementation in clinical settings is a key area for improvement. Finally, expanding the dataset and integrating more advanced TL models could improve model robustness and accuracy across a broader range of medical imaging conditions.

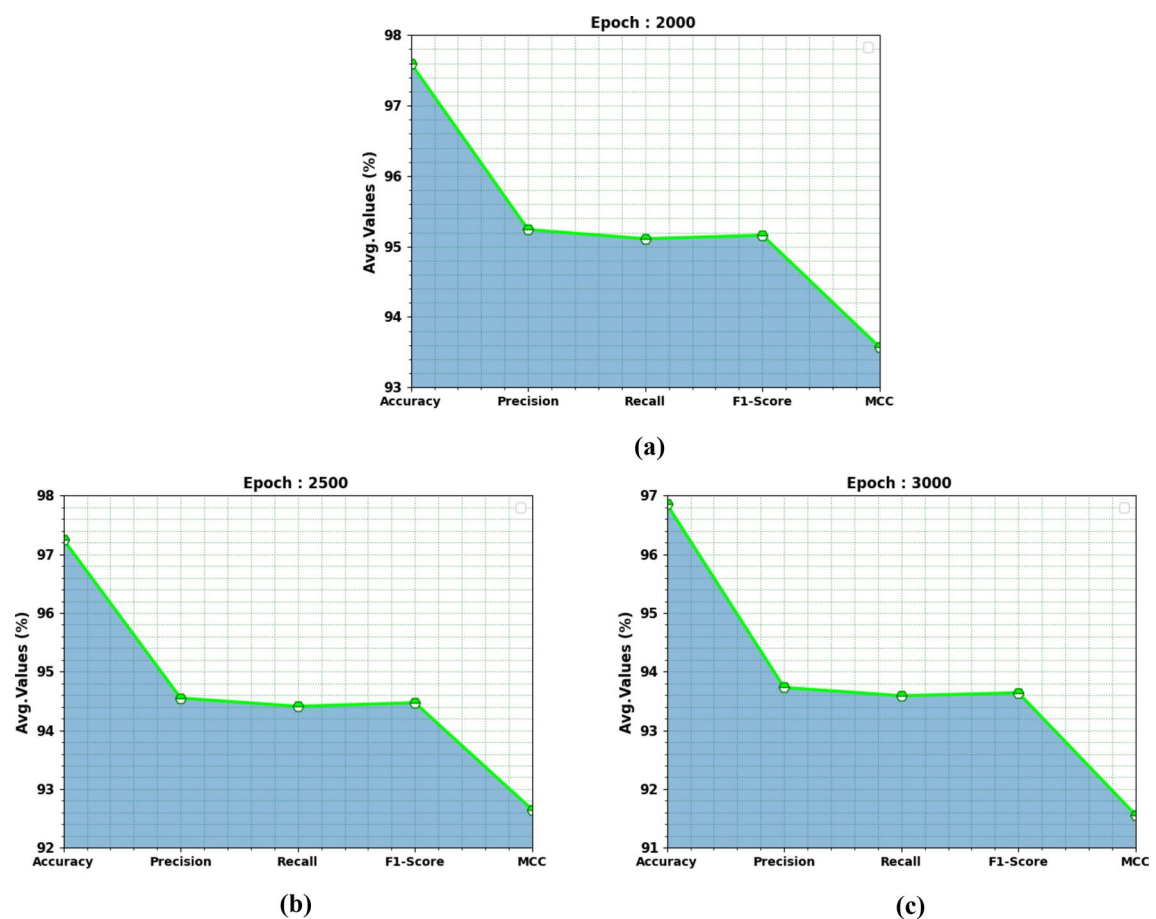


Fig. 10. Average outcome of XAISS-BMLBT approach (a–c) epochs 2000–3000.

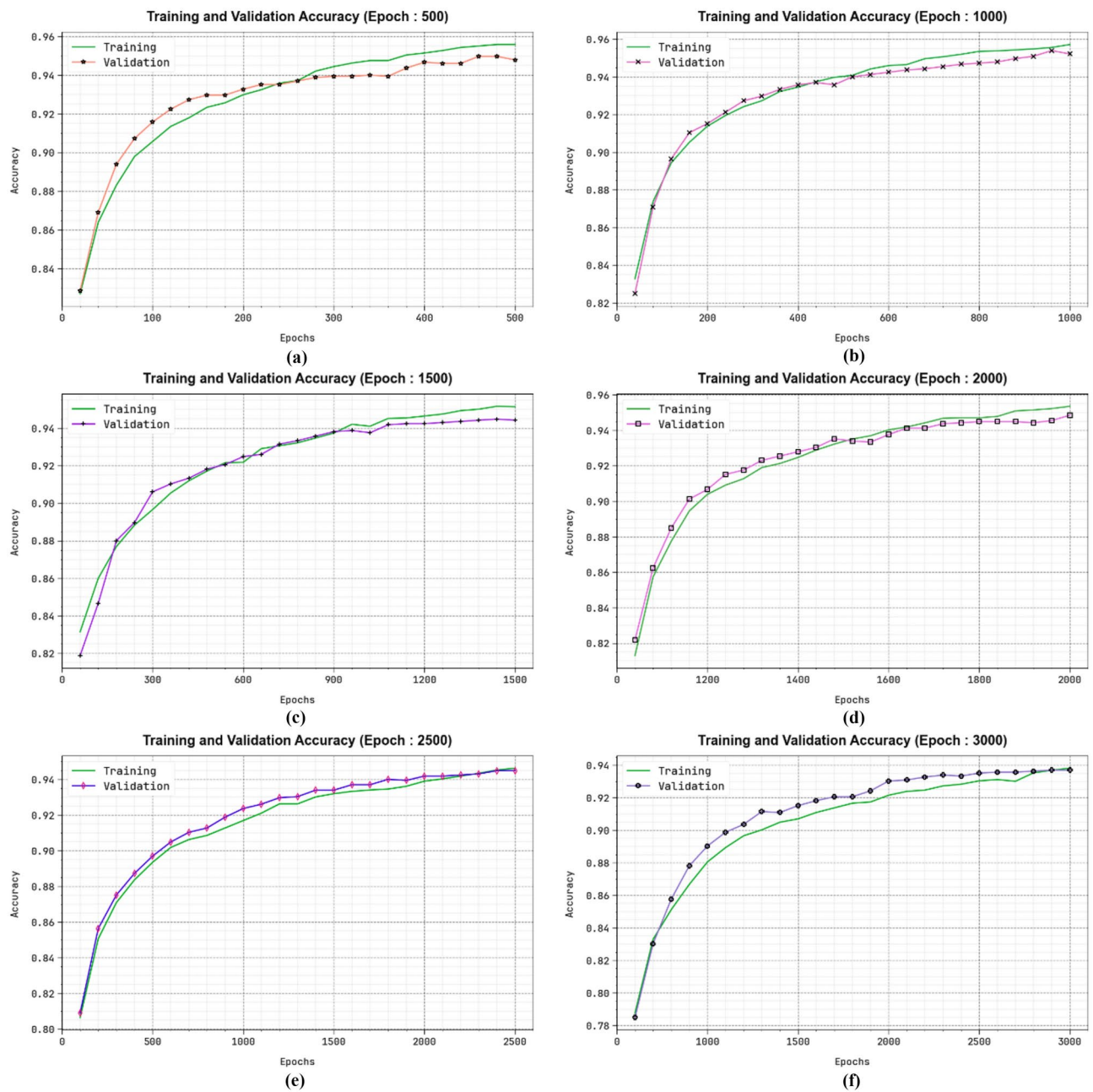


Fig. 11. $Accu_y$ curve of XAISS-BMLBT technique (a–f) Epochs 500–3000.

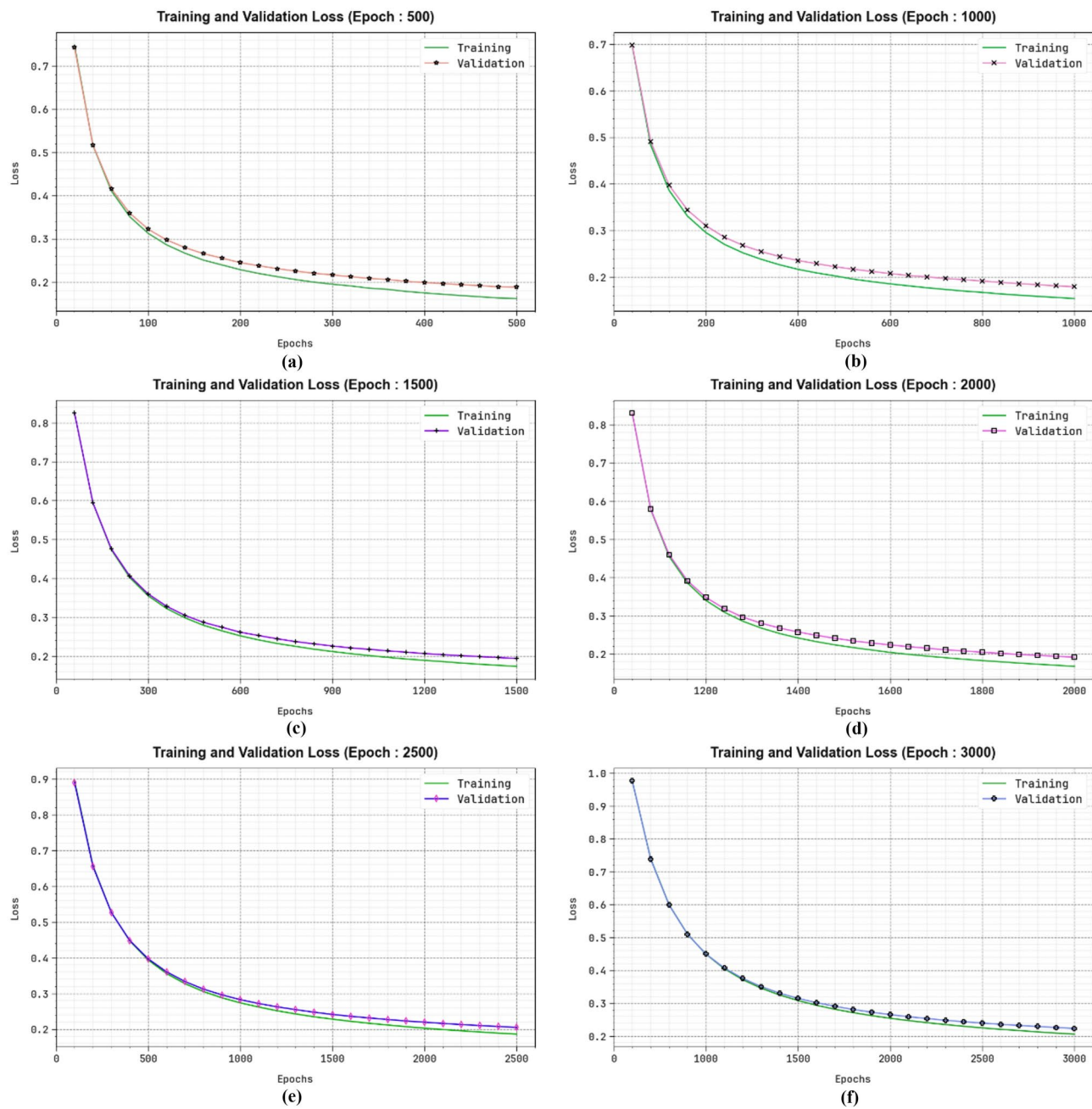


Fig. 12. Loss curve of XAISS-BMLBT technique (a–f) Epochs 500–3000.

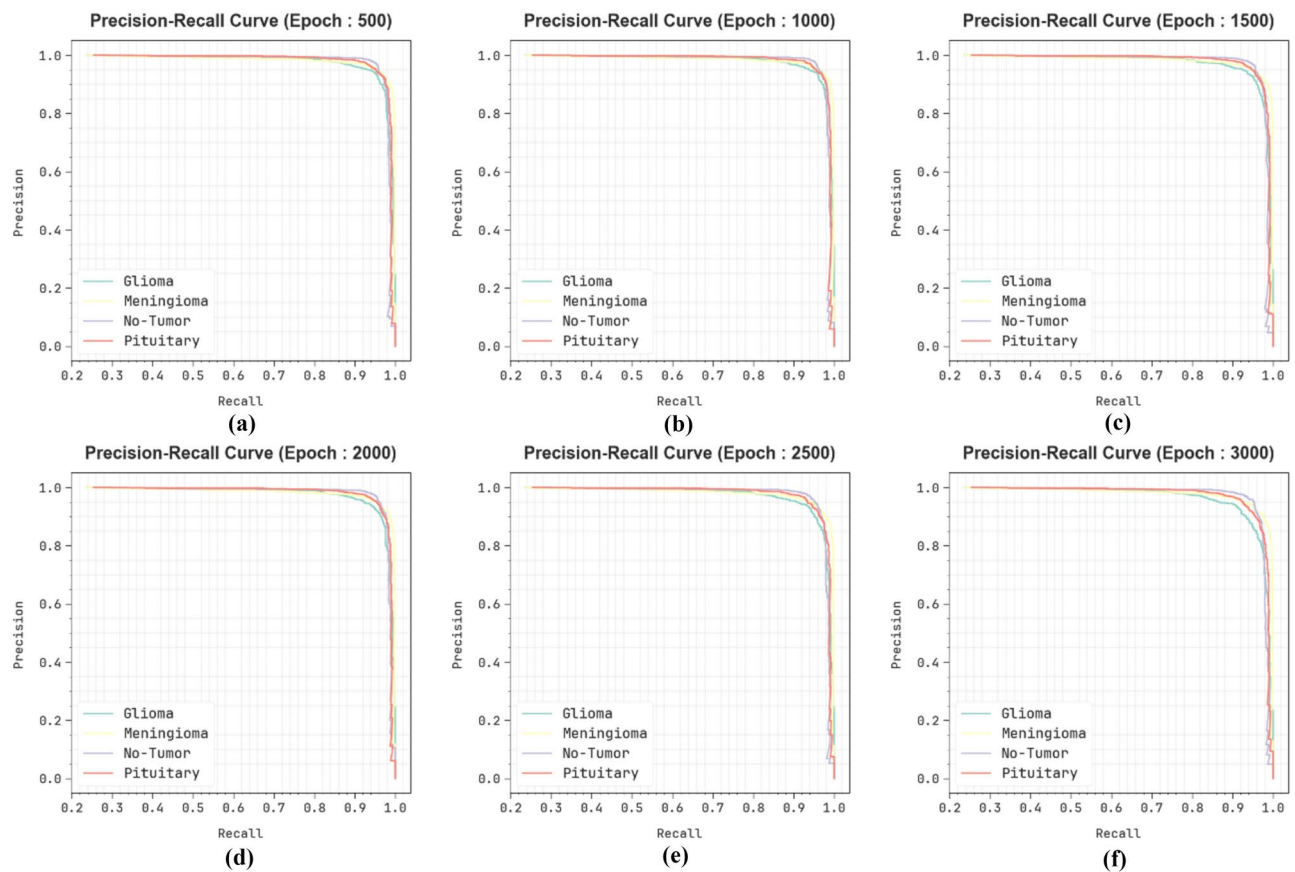


Fig. 13. PR curve of XAISS-BMLBT technique (a–f) Epochs 500–3000.

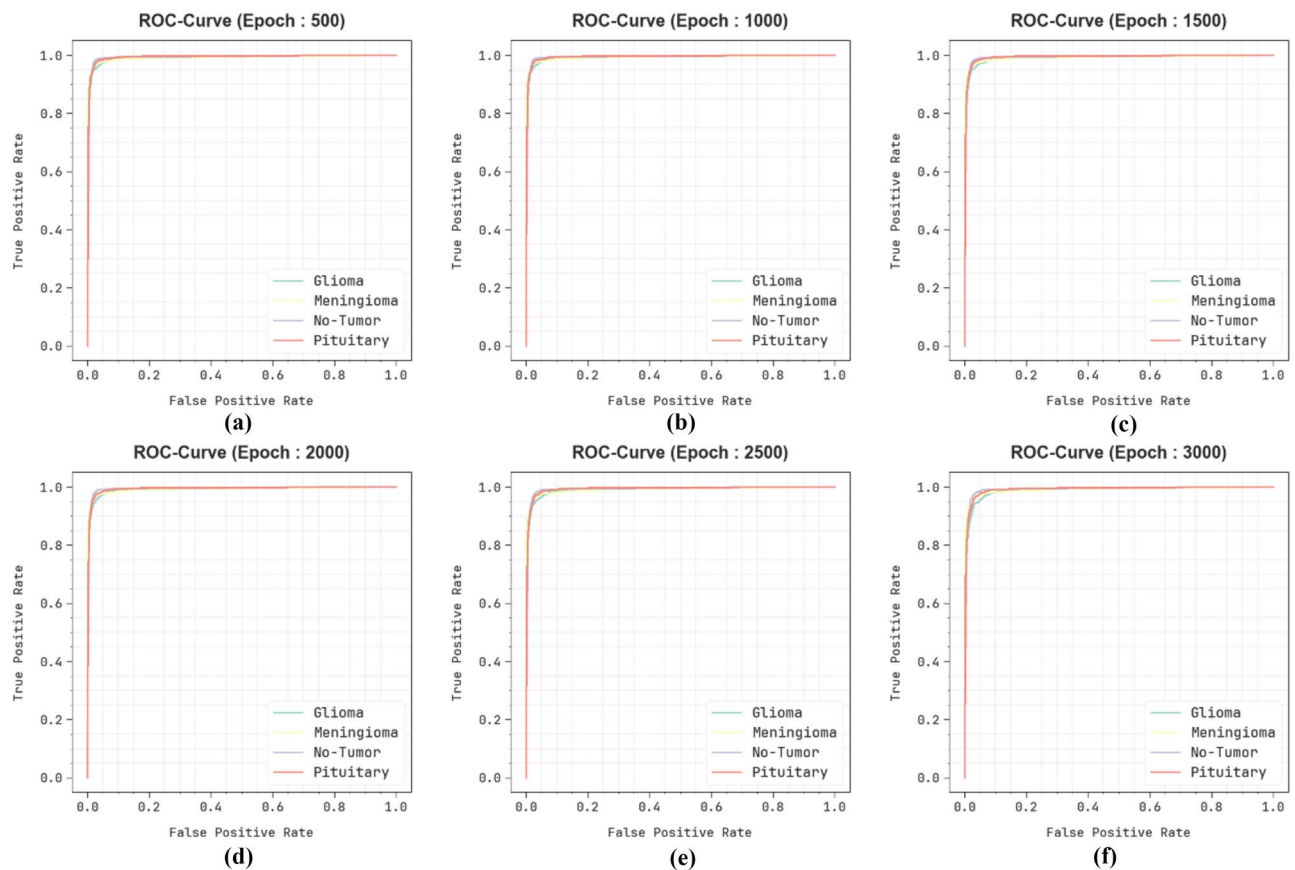


Fig. 14. ROC curve of XAISS-BMLBT technique (a–f) Epochs 500–3000.

Models	<i>Accu_y</i>	<i>Prec_n</i>	<i>Reca_I</i>	<i>F1_{Score}</i>
XAISS-BMLBT	97.75	95.56	95.42	95.48
Graph CNN	96.65	93.30	91.78	92.32
RF	95.96	94.23	94.02	91.46
Novel 3D-CNN	89.50	92.02	90.40	91.50
Inception-V3	95.60	94.01	94.15	92.18
Fine-tuned VGG19	94.00	93.03	91.71	92.95
ResNet50 model	96.50	94.41	91.04	94.86
Xception classifier	95.60	90.46	92.04	90.32
EfficientNet-B5	94.85	89.84	91.39	89.54
DenseNet-169	94.14	89.26	90.65	89.02
RanMerFormer	93.44	88.72	89.96	88.24
ResNet152V2	92.79	87.98	89.30	87.68

Table 3. Comparative analysis of XAISS-BMLBT technique with existing methods^{23,24,53–55}.

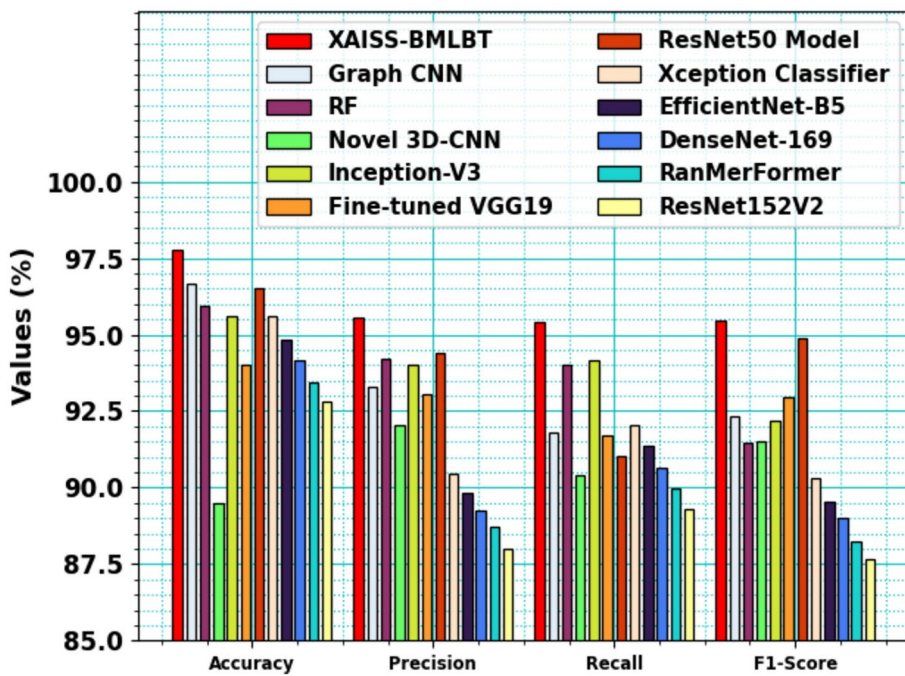


Fig. 15. Comparative analysis of XAISS-BMLBT technique with existing methods.

Models	EXT (s)
XAISS-BMLBT	4.60
Graph CNN	12.43
RF	9.77
Novel 3D-CNN	23.75
Inception-V3	19.08
Fine-tuned VGG19	16.92
ResNet50 model	18.73
Xception classifier	22.14
EfficientNet-B5	23.92
DenseNet-169	25.58
RanMerFormer	27.12
ResNet152V2	28.68

Table 4. EXT analysis of XAISS-BMLBT technique with existing methods.

Data availability

The data that support the findings of this study are publicly available at <https://www.kaggle.com/datasets/masoudnickparvar/brain-tumor-mri-dataset> (reference number⁵²).

Received: 26 August 2024; Accepted: 26 December 2024

Published online: 03 January 2025

References

- Mostafa, N. N. Human brain tumors detection using neutrosophic c-means clustering algorithm. *J. Neutrosophic Fuzzy Syst.* **1**(1), 55–65 (2021).
- Lu, S. Y., Satapathy, S. C., Wang, S. H. & Zhang, Y. D. PBTNet: A new computer-aided diagnosis system for detecting primary brain tumors. *Front. Cell Dev. Biol.* **9**, 765654 (2021).
- Gaur, L., Bhandari, M., Razdan, T., Mallik, S. & Zhao, Z. Explanation-driven deep learning model for prediction of brain tumour status using MRI image data. *Front. Genet.* **13**, 448 (2022).
- Hussain, T., Ullah, A., Haroon, U., Muhammad, K. & Baik, S. W. A comparative analysis of efficient CNN-based brain tumor classification models. In *Generalization with Deep Learning: For Improvement on Sensing Capability*, 259–278 (2021).
- Virupakshappa, & Amarapur, B. Computer-aided diagnosis applied to MRI images of brain tumor using cognition based modified level set and optimized ANN classifier. *Multimed. Tools Appl.* **79**(5–6), 3571–3599 (2020).
- Benyamina, H., Mubarak, A. S. & Al-Turjman, F. Explainable convolutional neural network for brain tumor classification via MRI images. In *2022 International Conference on Artificial Intelligence of Things and Crowdsensing (AIoTCs)*, 266–272 (IEEE, 2022).

7. Ali, S. et al. A comprehensive survey on brain tumor diagnosis using deep learning and emerging hybrid techniques with multimodal MR image. *Arch. Comput. Methods Eng.* **29**(7), 4871–4896 (2022).
8. Kumar, A., Manikandan, R., Kose, U., Gupta, D. & Satapathy, S. C. Doctor's dilemma: Evaluating an explainable subtractive spatial lightweight convolutional neural network for brain tumor diagnosis. *ACM Trans. Multimed. Comput. Commun. Appl. TOMM* **17**(3), 1–26 (2021).
9. Liu, T., Yuan, Z., Wu, L. & Badami, B. Optimal brain tumor diagnosis based on deep learning and balanced sparrow search algorithm. *Int. J. Imaging Syst. Technol.* **31**(4), 1921–1935 (2021).
10. Yu, L., Yu, Z., Sun, L., Zhu, L. & Geng, D. A brain tumor computer-aided diagnosis method with automatic lesion segmentation and ensemble decision strategy. *Front. Med.* **10**, 1232496 (2023).
11. Cekic, E., Pinar, E., Pinar, M. & Dagcinar, A. Deep learning-assisted segmentation and classification of brain tumor types on magnetic resonance and surgical microscope images. *World Neurosurg.* **182**, e196–e204 (2024).
12. Haq, E. U., Jianjun, H., Li, K., Haq, H. U. & Zhang, T. An MRI-based deep learning approach for efficient classification of brain tumors. *J. Ambient Intell. Humaniz. Comput.* **14**, 1–22 (2023).
13. Rajendran, S. et al. Automated segmentation of brain tumor MRI images using deep learning. *IEEE Access* **11**, 64758–64768 (2023).
14. Jyothi, P. & Singh, A. R. Deep learning models and traditional automated techniques for brain tumor segmentation in MRI: A review. *Artif. Intell. Rev.* **56**(4), 2923–2969 (2023).
15. Akter, A. et al. Robust clinical applicable CNN and U-Net based algorithm for MRI classification and segmentation for brain tumor. *Expert Syst. Appl.* **238**, 122347 (2024).
16. Anantharajan, S., Gunasekaran, S., Subramanian, T. & Venkatesh, R. MRI brain tumor detection using deep learning and machine learning approaches. *Meas. Sens.* **31**, 101026 (2024).
17. Mohanty, B. C., Subudhi, P. K., Dash, R. & Mohanty, B. Feature-enhanced deep learning technique with soft attention for MRI-based brain tumor classification. *Int. J. Inf. Technol.* **16**(3), 1617–1626 (2024).
18. Mehnatkesh, H., Jalali, S. M. J., Khosravi, A. & Nahavandi, S. An intelligent driven deep residual learning framework for brain tumor classification using MRI images. *Expert Syst. Appl.* **213**, 119087 (2023).
19. Amiya, G., Murugan, P. R., Ramaraj, K., Govindaraj, V., Vasudevan, M., Thirumurugan, M., Zhang, Y. D., Abdullah, S. S. & Thiagarajan, A. Expedited detection and segmentation of bone mass variation in DEXA images using the hybrid GLCM-AlexNet approach. *Soft Comput.* 1–14 (2024).
20. Subramanian, R. R. & Govindaraj, V. HARNet: Design and evaluation of a deep genetic algorithm for recognizing yoga postures. *Signal Image Video Process.* <https://doi.org/10.1007/s11760-024-03173-6> (2024).
21. Amiya, G. et al. LMGU-NET: Methodological intervention for prediction of bone health for clinical recommendations. *J. Supercomput.* **80**, 1–28 (2024).
22. Shi, F., Wang, J. & Govindaraj, V. SGS: SqueezeNet-guided Gaussian-kernel SVM for COVID-19 diagnosis. *Mob. Netw. Appl.* <https://doi.org/10.1007/s11036-023-02288-3> (2024).
23. Bouguerra, O., Attallah, B. & Brik, Y. MRI-based brain tumor ensemble classification using two stage score level fusion and CNN models. *Egypt. Inform. J.* **28**, 100565 (2024).
24. Wang, J., Lu, S. Y., Wang, S. H. & Zhang, Y. D. RanMerFormer: Randomized vision transformer with token merging for brain tumor classification. *Neurocomputing* **573**, 127216 (2024).
25. Saeed, T. et al. Neuro-XAI: Explainable deep learning framework based on deeplabV3+ and bayesian optimization for segmentation and classification of brain tumor in MRI scans. *J. Neurosci. Methods* **410**, 110247 (2024).
26. Alagarsamy, S., Govindaraj, V., Shahina, A. & Nagarajan, D. Intelligent multi-grade brain tumor identification in MRI: A metaheuristic-based uncertain set framework. *IEEE Trans. Artif. Intell.* **5**, 5381–5391 (2024).
27. Nisha, A. V. et al. Hybrid d-ocapnet: Automated multiclass Alzheimer's disease classification in brain MRI using hybrid dense optimal capsule network. *Int. J. Pattern Recognit. Artif. Intell.* **37**(15), 2356025 (2023).
28. Rahman, M. A. et al. GliomaCNN: An effective lightweight CNN model in assessment of classifying brain tumor from magnetic resonance images using explainable AI. *CMES-Comput. Model. Eng. Sci.* **140**(3), 2425–2448 (2024).
29. Alagarsamy, S., Govindaraj, V. & Senthilkumar, A. Automated brain tumor segmentation for MR brain images using artificial bee colony combined with interval type-II fuzzy technique. *IEEE Trans. Ind. Inform.* **19**(11), 11150–11159 (2023).
30. Charabi, H., Sayari, A., El Hamdi, R., Njah, M. & Slima, M. B. An XAI-infused multiclass MRI brain tumor classification using deep transfert learning (DTL). In *2024 10th International Conference on Control, Decision and Information Technologies (CoDIT)*, 1044–1049 (IEEE, 2024).
31. Rajeev, S. K., Rajasekaran, M. P., Vishnuvarthan, G. & Arunprasath, T. A biologically-inspired hybrid deep learning approach for brain tumor classification from magnetic resonance imaging using improved gabor wavelet transform and Elmann-BiLSTM network. *Biomed. Signal Process. Control* **78**, 103949 (2022).
32. Hosny, K. M., Mohammed, M. A., Salama, R. A. & Elshewy, A. M. Explainable ensemble deep learning-based model for brain tumor detection and classification. *Neural Comput. Appl.* <https://doi.org/10.1007/s00521-024-10401-0> (2024).
33. Mallampati, B. et al. Brain tumor detection using 3D-UNet segmentation features and hybrid machine learning model. *IEEE Access* **11**, 135020–135034 (2023).
34. Khosravi, P., Mohammadi, S., Zahiri, F., Khodarahmi, M. & Zahiri, J. AI-enhanced detection of clinically relevant structural and functional anomalies in MRI: Traversing the landscape of conventional to explainable approaches. *J. Magn. Reson. Imaging* **60**, 2272–2289 (2024).
35. Hossain, S., Chakrabarty, A., Gadekallu, T. R., Alazab, M. & Piran, M. J. Vision transformers, ensemble model, and transfer learning leveraging explainable AI for brain tumor detection and classification. *IEEE J. Biomed. Health Inform.* **28**(3), 1261–1272 (2023).
36. Nag, A. et al. TumorGANet: A transfer learning and generative adversarial network-based data augmentation model for brain tumor classification. *IEEE Access* **12**, 103060–103081 (2024).
37. Halder, A., Choudhuri, R. & Sarkar, A. Automated brain tumor analysis using deep learning-based framework. In *Medical Data Analysis and Processing using Explainable Artificial Intelligence*, 123–148 (CRC Press, 2023).
38. Lamba, K. & Rani, S. A novel approach of brain-computer interfacing (BCI) and Grad-CAM based explainable artificial intelligence: Use case scenario for smart healthcare. *J. Neurosci. Methods* **408**, 110159 (2024).
39. Roy, S., Pal, D. & Meena, T. Explainable artificial intelligence to increase transparency for revolutionizing healthcare ecosystem and the road ahead. *Netw. Model. Anal. Health Inform. Bioinform.* **13**(1), 4 (2023).
40. Chauhan, A. S. et al. Design and assessment of improved convolutional neural network based brain tumor segmentation and classification system. *J. Integr. Sci. Technol.* **12**(4), 793–793 (2024).
41. Bidkar, P. S., Kumar, R. & Ghosh, A. Hybrid Adam sewing training optimization enabled deep learning for brain tumor segmentation and classification using MRI images. *Comput. Methods Biomed. Eng. Imaging Vis.* **11**(5), 1921–1936 (2023).
42. Shafiq, M. U. & Butt, A. I. Segmentation of brain MRI using U-Net: Innovations in medical image processing. *J. Comput. Inform. Bus.* **1**(1) (2024).
43. Nirmalapriya, G., Agalya, V., Regunathan, R. & Ananth, M. B. J. Fractional Aquila spider monkey optimization based deep learning network for classification of brain tumor. *Biomed. Signal Process. Control* **79**, 104017 (2023).
44. Mithun, M. S. & Jawhar, S. J. Detection and classification on MRI images of brain tumor using YOLO NAS deep learning model. *J. Radiat. Res. Appl. Sci.* **17**(4), 101113 (2024).

45. Cao, Y. et al. MBANet: A 3D convolutional neural network with multi-branch attention for brain tumor segmentation from MRI images. *Biomed. Signal Process. Control* **80**, 104296 (2023).
46. Spagnolo, F., Corsonello, P., Frustaci, F. & Perri, S. Approximate bilateral filters for real-time and low-energy imaging applications on FPGAs. *J. Supercomput.* **80**, 1–23 (2024).
47. Yang, Z., Sun, X., Yang, Y. & Wu, X. MEDU-Net+: A novel improved U-Net based on multi-scale encoder-decoder for medical image segmentation. *KSII Trans. Internet Inform. Syst.* **18**, 1706–1725 (2024).
48. Nair, S. S. & Subaji, M. Automated identification of breast cancer type using novel multipath transfer learning and ensemble of classifier. *IEEE Access* **12**, 87560–87578 (2024).
49. Truong, T. T. et al. Data-driven prediction of tool wear using Bayesian regularized artificial neural networks. *Measurement* **238**, 115303 (2024).
50. Xi, L., Jin, L., Ji, Y., Liu, P. & Wei, J. Prediction of ultimate bearing capacity of soil-cement mixed pile composite foundation using SA-IRMO-BPNN model. *Mathematics* **12**(11), 1701 (2024).
51. Ashry, E. R., Maghraby, F. A., El-Latif, Y. M. A. & Agag, M. Pediatric posterior fossa tumors classification and explanation-driven with explainable artificial intelligence models. *Int. J. Comput. Intell. Syst.* **17**(1), 166 (2024).
52. <https://www.kaggle.com/datasets/masoudnickparvar/brain-tumor-mri-dataset>.
53. Jamalullah, R. S. et al. Leveraging brain MRI for biomedical Alzheimer's disease diagnosis using enhanced manta ray foraging optimization based deep learning. *IEEE Access* **11**, 81921–81929 (2023).
54. Vaiyapuri, T. et al. Ensemble learning driven computer-aided diagnosis model for brain tumor classification on magnetic resonance imaging. *IEEE Access* **11**, 91398–91406 (2023).
55. Abdusalomov, A. B., Mukhiddinov, M. & Whangbo, T. K. Brain tumor detection based on deep learning approaches and magnetic resonance imaging. *Cancers* **15**(16), 4172 (2023).

Author contributions

K.L.: Conceptualization, investigation, writing-original draft. S.A.: Formal analysis, software, visualization. G.S.: Resources, investigation, software. S.P.: Data curation, methodology, validation. G.P.J.: Validation, supervision, writing-review and editing. W.C.: Funding acquisition, project administration, supervision.

Declarations

Competing interests

The authors declare no competing interests.

Ethics approval

This article contains no studies with human participants performed by any authors.

Additional information

Correspondence and requests for materials should be addressed to G.P.J. or W.C.

Reprints and permissions information is available at www.nature.com/reprints.

Publisher's note Springer Nature remains neutral with regard to jurisdictional claims in published maps and institutional affiliations.

Open Access This article is licensed under a Creative Commons Attribution-NonCommercial-NoDerivatives 4.0 International License, which permits any non-commercial use, sharing, distribution and reproduction in any medium or format, as long as you give appropriate credit to the original author(s) and the source, provide a link to the Creative Commons licence, and indicate if you modified the licensed material. You do not have permission under this licence to share adapted material derived from this article or parts of it. The images or other third party material in this article are included in the article's Creative Commons licence, unless indicated otherwise in a credit line to the material. If material is not included in the article's Creative Commons licence and your intended use is not permitted by statutory regulation or exceeds the permitted use, you will need to obtain permission directly from the copyright holder. To view a copy of this licence, visit <http://creativecommons.org/licenses/by-nc-nd/4.0/>.

© The Author(s) 2025